

www.acsanm.org Article

Interfacial and Bulk Assembly of Anisotropic Gold Nanostructures: Implications for Photonics and Plasmonics

Hyeong Jin Kim, Md Mir Hossen, Andrew C. Hillier, David Vaknin, Surya K. Mallapragada,* and Wenjie Wang*



Cite This: ACS Appl. Nano Mater. 2020, 3, 8216-8223



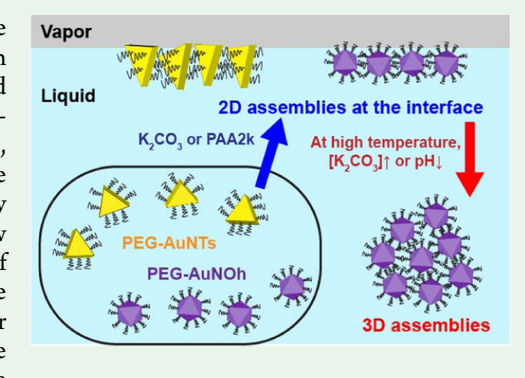
ACCESS

Metrics & More



Supporting Information

ABSTRACT: We report on the assembly of polymer-grafted nanostructures at the vapor/aqueous interface and in bulk solutions using synchrotron X-ray diffraction methods. Triangular- and octahedral-shaped gold nanostructures are synthesized and grafted with poly(ethylene glycol) (referred to as PEG-AuNTs and PEG-AuNOh, respectively), and their suspensions are manipulated with salts, (poly)electrolytes that induce interpolymer complexation and HCl to achieve organized assemblies. The assemblies at the vapor/liquid interface are explored by X-ray reflectivity and grazing-incidence small-angle X-ray scattering. Results show that PEG-AuNTs and PEG-AuNOh populate the interface, with some degree of orientation with respect to the liquid surface. The resulting assemblies can be tuned by the regulating electrolyte and pH levels of the suspensions. Similar suspension manipulations also induce three-dimensional assemblies that are revealed with solution small-angle X-ray scattering. In addition to controlling the



three-dimensional (3D) aggregates by regulating the (poly)electrolytes and pH levels, we show that raising the temperature of the suspensions from 20 to above 50 °C induces and even improves the ordering of the assemblies. Our findings provide tools that can be used to assemble and orient anisotropic nanostructures for potential applications in photonics and plasmonics.

KEYWORDS: assembling nanostructures, salt-induced self-assembly, interpolymer complexation, PEG-grafted gold nanostructures, X-ray reflectivity (XRR), grazing-incidence small-angle X-ray scattering (GISAXS), small-angle X-ray scattering (SAXS)

■ INTRODUCTION

Progress in the synthesis of nanoparticles has led to the fabrication of functional nanoscale building blocks for ordered assemblies with novel collective properties that are applicable in photonics, plasmonics, electronics, catalysis, and sensing. 1-12 Owing to their unique and appealing properties, various strategies for nanostructure assembly and crystallization have been developed through the interplay of electrostatic, hydrogen bonding, van der Waals (vdW) interactions, hydrophobic effect, antigen-antibody (i.e., lock-and-key) recognition, and DNA hybridization. Recently, a series of systematic studies demonstrated the assembly and crystallization of gold nanoparticles (AuNPs) that are grafted with water-soluble polymers, such as poly(ethylene) glycol (PEG),^{22–28} and poly(N-isopropylacrylamide) (PNIPAM).²⁹ The PEG-grafted AuNPs are soluble and well dispersed in aqueous solutions in the absence of electrolytes at or near neutral pH. However, adding salts to the suspensions induces assembly and ordering at the vapor/liquid interface and at higher concentrations creates ordered three-dimensional (3D) aggregates.^{23,24} In addition to the salt-mediated strategy, interpolymer complexation (IPC), using poly(acrylic acid) (PAA) in the suspension below its isoelectric point (pI), has been recently developed for the two-dimensional (2D) and 3D assembly of PEG-AuNPs. 30,31 Beyond traditional spherical nanoparticles, new opportunities are provided by developing strategies for self-assembly and crystallization of anisotropic nanostructures.^{32–41} The advantage of using anisotropic nanoobjects is that their distinct properties can be achieved by manipulating their shape and/or size. The desired local properties of the individual particles can be furthermore exploited in their collective behaviors as assembled ordered structures, potentially in optical devices and metamaterials. 42-44 Recently, DNA-mediated gold nanocube arrays have been investigated to control the structural and optoelectronic properties with respect to nanostructure shape, size, and spacing of particles for advanced photonic metamaterials. Nevertheless, the assembly of anisotropic nanostructures remains a challenge, compared to the assembly of isotropic nanoparticles. 45,46 Here, we report on the assembly of PEGgrafted nanotriangles (NTs) and nano-octahedra (NOh) in

Received: June 15, 2020 **Accepted:** July 16, 2020 **Published:** July 16, 2020





salt or PAA suspensions at the vapor/liquid interfaces⁴⁷ and in the bulk, as illustrated in Figure 1.

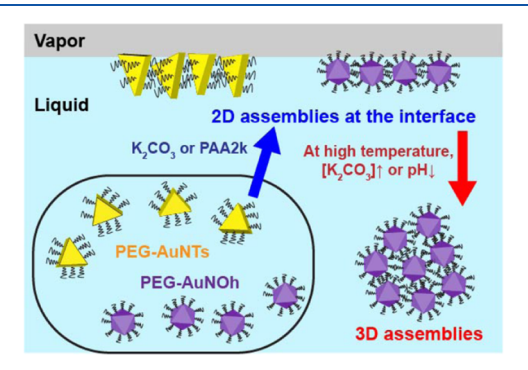


Figure 1. Schematic illustration of 2D and 3D assemblies of PEG-AuNTs and PEG-AuNOh at the vapor/liquid interface and in the bulk mediated with salt or interpolymer complexation (IPC).

EXPERIMENTAL DETAILS

Materials and Methods. Gold(III) chloride trihydrate (HAuCl₄· $3H_2O$, $\geq 99.9\%$), benzyldimethylhexadecylammonium chloride (BDAC), hexadecyltrimethylammonium chloride (CTAC, $\geq 98.0\%$), 3-butenoic acid (BA, $\geq 97\%$), and poly(acrylic acid) with an average molecular weight (M_w) of ~ 2 kDa (referred to as PAA2k or PAA without specification) were purchased from Sigma-Aldrich and used as received. Poly(ethylene glycol) methyl ether thiol (mPEG-SH) with M_w of ~ 5 and ~ 10 kDa (referred to as PEG5k and PEG10k, respectively) were obtained from CreativePEGWorks.

Gold nanotriangles (AuNTs) and nano-octahedra (AuNOh) are fabricated following the procedure described in the literature. ^{48–50} In a typical synthesis, HAuCl₄ and BDAC are mixed in a 20 mL glass vial to give 10 mL of a solution containing 0.5 mM HAuCl₄ and 5 mM BDAC. The thoroughly mixed solution is heated to ~75 °C on a hot plate to which 10 μ L of BA is added followed by a stirring process. Subsequently, the color of the solution changes to dark pink, indicating the formation of gold nanostructures. The solution vial is then removed from the hot plate and cooled to room temperature. UV-visible spectra of the solution measured with a Nanodrop One is used to verify the formation of gold nanostructures. The as-prepared nanoparticles solution is then centrifuged at 10 000 rpm in a Eppendorf MiniSpin Plus to remove the excess of BA and BDAC. We note that at this stage, the as-synthesized nanostructure solution contains both AuNTs and AuNOh. To separate the AuNTs and AuNOh, 350 mM CTAC is added to the mixture and then kept overnight on a bench, during which a precipitate of AuNTs and supernatant of AuNOh are formed. The supernatant is transferred to a fresh centrifuge tube, and AuNTs are resuspended in nanopure water.

It is notoriously difficult to perfectly separate AuNTs and AuNOh at this stage. However, the major nanostructures in the precipitate and supernatant are AuNTs and AuNOh, respectively (see more detail in Table 1). Both AuNTs and AuNOh are nanosized structures (NSt) and are referred to as AuNSts in general without context. Synthesized AuNTs and AuNOh are grafted with PEG10k and PEG5k through a ligand exchange process and centrifugation as described elsewhere ⁴⁷ and are referred to as PEG-AuNTs and PEG-AuNOh, respectively.

Dynamic light scattering (DLS; Nano ZS90, ZEN3690) is used to determine the hydrodynamic size distribution of the nanoparticles in bulk solutions (Figure S1). The calculated hydrodynamic size distribution of AuNTs and AuNOh is hindered because of the inevitable entanglement of translational and rotational diffusion of nonspherical nanostructures. Therefore, the measurement does not provide direct information of their actual sizes.⁵¹ Nevertheless, DLS measurements show significant changes between the bare and the PEG-grafted nanostructures manifested by an effective increase in size. This confirms the grafting of PEG on the facets of AuNSts and also that PEG-AuNSts are well dispersed in the suspensions (see more details in the Supporting Information, Figure S1).⁴⁷ Figure S2 shows the UV-visible spectra (SpectraMax M3, Molecular Devices) of PEG-AuNSts dispersed in the bulk solution. The surface plasmon resonance peaks (λ_{max}) of PEG-AuNTs and PEG-AuNOh are at ~580 and ~550 nm, respectively, in agreement with previous reports.⁴⁹ The shift to the longer wavelength ~580 nm for PEG-AuNTs is consistent with their average size being larger than PEG-AuNOh, 52 which is also confirmed by scanning electron microscopy (SEM) and transmission electron microscopy (TEM). UV-visible spectra are also used to estimate the concentration of PEG-AuNSts using Beer's law.

For characterization of the morphology and size distribution, PEG-AuNSts are deposited on RCA cleaned n-type silicon.⁵³ Then, a field emission scanning electron microscopy (FE-Teneo, operated at 20 kV) in high-vacuum mode is used to image PEG-AuNSts. Representative SEM images of PEG-AuNTs and PEG-AuNOh are shown in Figure 2a,b after the separation process and grafting. Due to the PEG polymer covering the nanostructure surface, the SEM resolution is slightly diminished (see Figure S3 for more details on the morphology of gold nanostructures). PEG-AuNTs and PEG-AuNOh aqueous solutions contain ~68% AuNTs of 45 ± 5.8 nm length and \sim 76% AuNOh of 28 \pm 3.4 nm size (the largest vertex-to-vertex distance), respectively (see more details in Table 1). TEM (FEI Tecnai G2 F20) is also used to image the morphology of PEG-AuNSts by depositing them on a TEM grid (Carbon type-B, 300 mesh, copper). TEM images for the representative individual nanostructures of PEG-AuNTs and PEG-AuNOh are shown in Figure 2c,d, respectively.

Synchrotron X-ray structural studies were performed at the Advanced Photon Source (APS), Argonne National Laboratory. The aqueous surface measurements, *i.e.*, liquid surface X-ray reflectivity (XRR) and grazing-incidence small-angle X-ray scattering (GISAXS) were carried out at the liquid surface spectrometer at

Table 1. Overview of the Information of AuNTs and AuNOh Used in This Study

	size and shape distribution a,b	functionalization of PEG	concentration	X-ray characterization	self-assembly method
AuNTs	triangles (\sim 68%) 45 ± 5.8 nm octahedra (\sim 31%)	PEG10k	~0.32 nM	XRR, GISAXS	salt, IPC
AuNOh	35.5 ± 4.5 nm triangles (~23%) 36 ± 3.6 nm octahedra (~76%)	PEGSk	~0.42 nM	SAXS XRR, GISAXS	IPC salt, IPC
	$28 \pm 3.4 \text{ nm}$		~1.08 nM	SAXS	salt, IPC

[&]quot;Quantification is based on the analysis of scanning electron microscopy (SEM) images. b Size of the AuNTs refers to its triangular base edge length as measured by SEM. Thickness (\leq 23 nm) of the AuNTs is estimated using atomic force microscopy. Size of the AuNOh refers to the largest vertex-to-vertex distance. In the Supporting Information, the small-angle X-ray scattering (SAXS) data analysis provides an alternative estimate on overall dimensions.

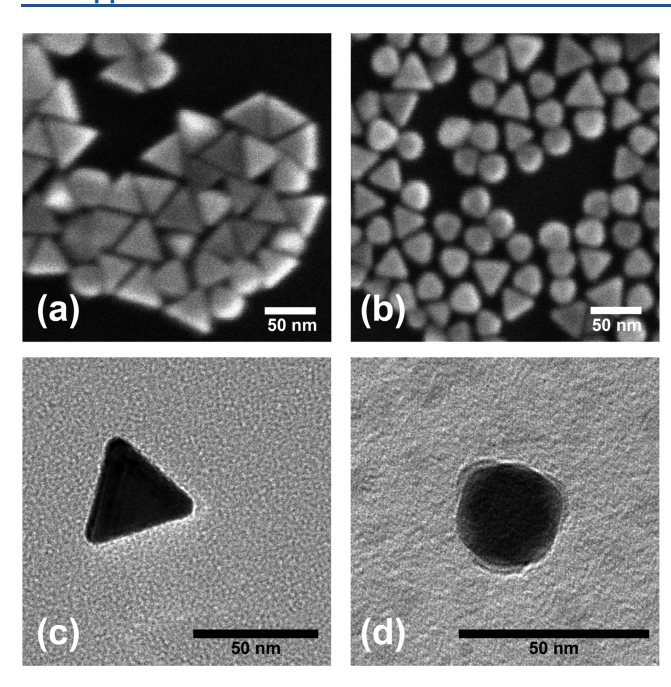


Figure 2. Representative SEM images of (a) PEG-AuNTs and (b) PEG-AuNOh. TEM images for individual (c) PEG-AuNT and (d) PEG-AuNOh.

beamline 15ID-C (APS), NSF's ChemMatCARS with X-ray energy 10 keV. The bulk characterization of the suspensions by small-angle X-ray scattering (SAXS) at X-ray energy 13.3 keV was conducted at beamline 12ID-B (APS). The experimental protocols in the two beamlines are similar to those already described elsewhere. 24,28,30,31,4 Briefly, the measured X-ray reflectivity, $R(Q_z)$, is a function of the vertical component of the scattering vector Q and displayed in our figures after normalization to the calculated Fresnel reflectivity, $R_{\rm F}$, for an ideally sharp and flat surface of the bulk solution. From the reflectivity, we determine the electron density (ED) profile, $\rho(z)$, across the interface by refining the parameters of $\rho(z)$ to obtain the best calculated fit to the measured reflectivity using the Parratt's recursive method (z-axis being along the surface normal).⁵⁴ The lateral packing structure of the NSts on the aqueous surface is probed via GISAXS. ^{28,31} For the GISAXS, the incident angle of the X-ray beam, α_{ν} is kept below the critical angle for total reflection, α_{c} . Here, the intensity versus Q_{xy} the horizontal component of \mathbf{Q}_t is integrated over Q_z from 0.02 to 0.1 Å⁻¹.

For SAXS measurements, the solutions are loaded in quartz capillaries and the sample temperature is controlled and monitored. Temperature is raised from 20 to 80 °C and then lowered back to 20 °C at a constant rate of 10 °C/min. At each 10 °C increment (or decrement), the temperature is maintained for 10 min to stabilize the sample. The SAXS intensity is expressed as a function of the magnitude of the scattering vector, $Q = |\mathbf{Q}|$, owing to the isotropy of the scattering pattern. The suspended NSts and their aggregates in the bulk of the solutions are characterized with SAXS following established procedures. ^{24,30,55}

RESULTS AND DISCUSSION

Two-Dimensional Interfacial Assembly of PEG-AuNTs and PEG-AuNOh. X-Ray Reflectivity (XRR). Normalized X-ray reflectivity data, R/R_F , are shown in panels (a) and (c) in Figure 3 for PEG-AuNTs and in Figure 4 for PEG-AuNOh under various controlled solvent conditions as indicated. Panels (b) and (d) show the corresponding electron density (ED) profiles that produce the best-fit to R/R_F data in (a) and (c), respectively. For both systems, in the absence of K_2CO_3 or PAA (and HCl), R/R_F is close to unity, indicating a liquid

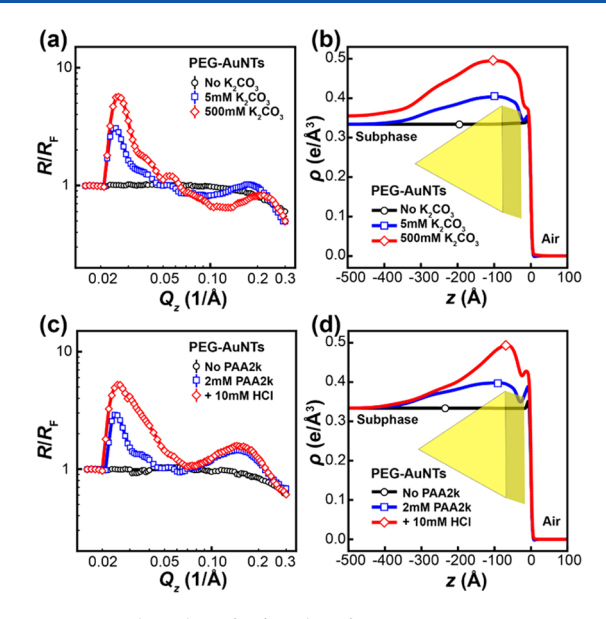


Figure 3. Log—log plot of $R/R_{\rm F}$ data for PEG-AuNT suspensions in response to varying concentration of (a) $K_2{\rm CO}_3$ or (c) HCl in the presence of 2 mM PAA2k. Their corresponding ED profiles (b, d) generate the best-fitting (solid lines) for $R/R_{\rm F}$ data in (a) and (c), respectively.

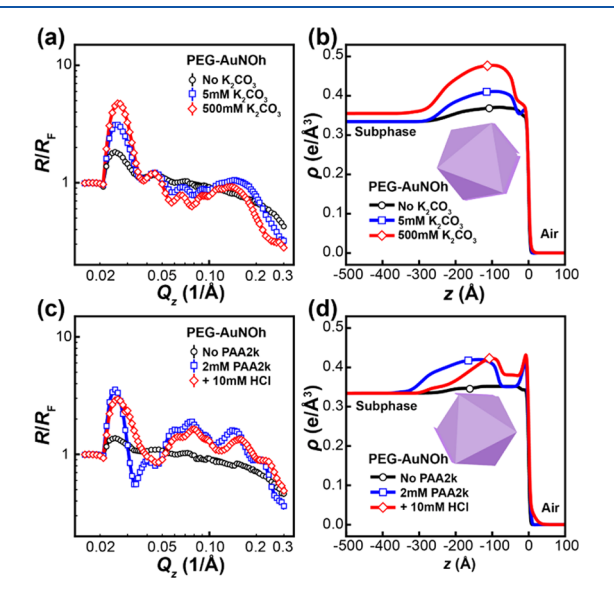


Figure 4. Log—log plot of $R/R_{\rm F}$ data for PEG-AuNOh suspensions in response to varying concentration of (a) $\rm K_2CO_3$ or (c) HCl in the presence of 2 mM PAA2k. Their corresponding ED profiles (b, d) generate the best-fitting (solid lines) for $R/R_{\rm F}$ data in (a) and (c), respectively.

surface with no accumulation of NSts. As more salt or PAA and HCl are added, $R/R_{\rm F}$ increases above 1, indicating surface electron enrichment due to a higher density of AuNSts at the vapor/liquid interface. The extracted ED profiles show the same trend, namely, enhancement in the region immediately adjacent to the vapor/liquid interface (i.e., z=0), indicating the migration of PEG-AuNSts to the aqueous surface in response to the addition of either salts (i.e., K_2CO_3) or PAA to the suspensions.

The ED enhanced segment along the z-axis extends within a depth that is comparable to the size of the AuNSts estimated by SAXS and SEM, as listed in Table 1 (see the Supporting

Table 2. Summary of XRR and GISAXS Analysis

			GISAXS			
nanostructures	conditions	$\Gamma_{ m e}$	CM-to-surface	dimension	skewness	peak presence
		$\left(e/\text{Å}^2\right)$	distance (nm)	2σ (nm)	$ ilde{\mu}_3$	
PEG-AuNTs	5 mM K ₂ CO ₃	16.1	15.8	17.6	-0.50	no
PEG-AuNTs	500 mM K ₂ CO ₃	32.8	15.8	17.6	-0.61	no
PEG-AuNTs	PAA	15.7	15.8	18.6	-0.43	no
PEG-AuNTs	PAA + 10 mM HCl	29.6	13.3	17.8	-0.82	yes
PEG-AuNOh	5 mM K ₂ CO ₃	14.3	12.5	12.8	-0.17	no
PEG-AuNOh	500 mM K ₂ CO ₃	23.2	13.6	13.2	-0.28	no
PEG-AuNOh	PAA	18.4	16.0	16.4	0.16	yes
PEG-AuNOh	PAA + 10 mM HCl	15.2	10.5	14.0	-0.33	yes

^aThe meaning of each of these four parameters derived from the XRR analysis is briefly described in the main text and the detailed discussion can found in the Supporting Information.

Information for more details). This reveals that a single layer of PEG-AuNSts is formed at the vapor/liquid interface. 23,25 We also observe that the shapes of the ED profiles (defined in the Supporting Information) exhibit asymmetry as may be expected from nonspherical AuNSts. The shape of the ED distribution can be quantified by their nth moments (mathematically defined in the Supporting Information), as summarized in Table 2. The zeroth moment is the surface electron density excess, $\Gamma_{\rm e}$, that is proportional to the surface excess of PEG-AuNSts. We note that the enhancement in the ED profile is primarily due to the AuNSts as the PEG has much lower ED than that of solid Au. The higher-order moment of distributions can be associated with the orientations of the specific AuNSt (e.g., Figures S4 and S5).

Our XRR analysis can be summarized as follows. (1) Adding salts (i.e., K₂CO₃) to the bulk solutions increases the surface activity of the PEG-AuNSts in suspension. In the presence of 5 mM K₂CO₃, the ED profile for PEG-AuNSt suspensions exhibits some ED enrichment compared to that of suspensions with no salt, indicating the onset of NSts interfacial aggregation. Increasing salt concentration by 2 orders of magnitude further doubles the surface excess of PEG-AuNSts (see Table 2). Such a qualitative trend of linear increase of surface-bound PEG-AuNSts concentration versus the logarithmic of bulk salt concentration has been observed for PEGgrafted spherical gold nanoparticles (PEG-AuNPs) in earlier studies.²³ The derived first moment (the center of mass, CM) and the second moment (σ^2) show that both PEG-AuNTs and PEG-AuNOh layers are very close to the average NSts size, thus validating a single-layer formation at the interface. Compared to the ED profile for a PEG-AuNP monolayer,²³ ED profiles for PEG-AuNTs exhibit asymmetry that can be associated with a partial preferred orientation at the surface. Here, the asymmetry is quantified with the third central normalized moment of the ED profile, known as skewness (see definition in the Supporting Information). The skewness of the ED profile for PEG-AuNTs is negative (≤ -0.5 ; in accordance with our chosen coordinate), indicating that the triangular prism orients at the surface (see Figure S6). We examine two orientations with respect to the surface. One orientation is "face-on" and the other is "base-on," as depicted in the Supporting Information. Based on simulations of the resulting ED profiles for thin triangular prisms adopting this binary orientation (see Figure S7), we suggest that salt/electrolyte induces PEG-AuNTs to adopt a face-on orientation, even for a denser monolayer at higher salt concentrations. The scenario that all AuNTs adopt a base-on orientation at the vapor/liquid

interface is less plausible; otherwise, it should lead to a more symmetric ED profile, namely, with much less skewness (i.e., close to zero). Although oriented, these salt-induced, surfaceanchored, face-on favored PEG-AuNTs are randomly arranged on the horizontal plane, lacking any sort of preferred in-plane ordering (see Grazing-Incidence Small-Angle X-ray Scattering discussion below and Figure S9). The skewness for PEG-AuNOh is much closer to zero, indicating much less deviation from spherical symmetry for octahedra. (2) Adding PAA/HCl to the bulk solution increases the surface activity of the PEG-AuNSts via IPC, and we suggest that NSts orientation is driven by maximizing vdW interparticle interfacial interactions. It has been shown that PAA, by tuning the bulk pH, promotes either two-dimensional assembly by IPC at the vapor/liquid interface or three-dimensional assembly in the bulk. 30,31 At neutral pH, PAA acts as a polyelectrolyte, thus mimicking the role of salts in driving the PEG-AuNSts to the aqueous surface. At low pH (below the pI of PAA, ≤ 4.5), ^{58,59} PAA-PEG complexation, initiated by hydrogen bonds, develops into more of vdW interaction and leads to the formation of stable aggregates void of water molecules in the PEG-corona.²⁷ Figures 3 and 4 show that IPC affects the orientations of the constituent PEG-AuNSts in the monolayers. Prior to lowering the pH, the electron distribution (and equivalently, mass distribution) is more distributed in the z-direction, leading to a larger CM-tosurface distance (for PEG-AuNOh in particular) and larger σ . The IPC formed at low pH leads to a distorted ED with shorter CM-to-surface distance, smaller σ , and larger negative skewness. These effects demonstrate that IPC is more efficient than simple salts at orienting anisotropic NSts at the vapor/ liquid interface. The narrow peak in the ED enhancement closer to the vapor interface is unusual, and we speculate it is likely due to a denser dehydrated PAA-PEG/IPC region. In general, IPC-induced surface assembly favors particulate alignment as shown in Grazing-Incidence Small-Angle X-ray Scattering below.

Grazing-Incidence Small-Angle X-ray Scattering (GISAXS). Two-dimensional GISAXS patterns provide information on the lateral packing of PEG-AuNSts at the vapor/liquid interface. Figure 5 shows GISAXS intensity versus Q_{xy} profiles for PEG-AuNSts suspensions in the presence of PAA2k for which IPC is enhanced at low pH.

For PEG-AuNTs, a diffraction peak corresponding to partial 2D ordering ($Q_{xy} \sim 0.0171$, 0.0188 Å⁻¹) emerges only after lowering the pH level by the addition of HCl to the suspension with 2 mM PAA2k (Figure 5a). We use the peak position to estimate that the average interparticle distance ($d = 2\pi/Q$)

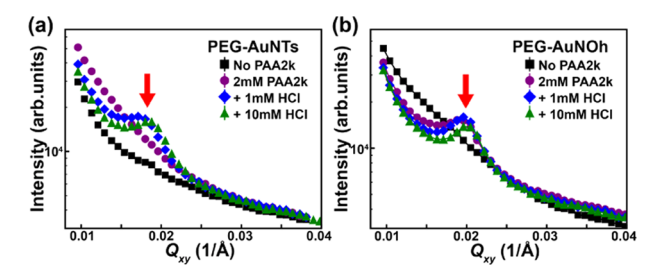


Figure 5. GISAXS intensity profiles integrated over $Q_z = 0.02-0.1$ Å⁻¹ for (a) PEG-AuNTs and (b) PEG-AuNOh suspensions with 2 mM PAA2k in response to the varying concentration of HCl. Red arrows indicate the diffraction peak.

among the PEG-AuNTs with 1 and 10 mM HCl is at ~37 and ~33 nm, respectively, given the length and thickness of AuNT (length \simeq 45 nm, thickness \leq 23 nm). These values and the estimated thickness of the PEG-corona surrounding the NSts ^{47,55} suggest that the PEG-AuNTs are mostly anchored face-on at the vapor/liquid interface (as illustrated in Figure 1) and consistent with the aforementioned XRR analysis. Figure 5b shows similar GISAXS patterns for PEG-AuNOh, implying only short-range order with ~33 to 32 nm interparticle distances at the increased HCl concentration in the presence of PAA2k. We note that GISAXS measurements with varying K_2CO_3 concentrations do not show any diffraction features for PEG-AuNSts, consistent with our conclusion based on the XRR that IPC is more effective at aligning and ordering PEG-AuNSts at the vapor/liquid interface (Figure S9).

Three-Dimensional Assembly of PEG-AuNTs and PEG-AuNOh in the Bulk. We explore the 3D assembly of PEG-AuNSts in bulk solutions using SAXS measurements. To analyze the diffraction patterns, the structure factor is extracted by dividing the SAXS intensity by the form factor of PEG-AuNSts (see form factors of both NSts in Figure S8). Figure S10 shows the SAXS structure factor profiles for PEG-AuNTs suspensions at 2 mM PAA2k at various pH levels. Short-range order is extracted from the patterns at 0 and 1 mM HCl concentrations in the presence of PAA2k, and the interparticle distance decreases with the increase of HCl, similar to the behavior at the vapor/liquid interface (Figure S10, see more details in the Supporting Information).

Effect of Temperature on the 3D Assembly of PEG-AuNOh. Salt Induced. For 50 mM K2CO3, no features are observed in the structure factor profiles of PEG-AuNOh at the temperature range of 20-80 °C (Figure S11). Figure 6a shows the SAXS structure factor for PEG-AuNOh suspensions at 500 mM K₂CO₃ at various temperatures. Temperature is raised from 20 to 80 °C and then lowered back to 20 °C at a constant rate. A strong diffraction pattern emerges at about 50 °C signaling the formation of 3D assemblies in the bulk. Interestingly, as the temperature increases further, the primary peak (Q_1) gradually shifts to larger values, indicating the counterintuitive contraction of the interparticle distance (see Figure S12a). Lowering the temperature back to 20 °C, the fundamental peak at Q_1 is still intense but shifts to lower values (sky blue square profile in Figure 6a), evidence of the irreversibility of the assemblies, albeit at a looser packing. This result is consistent with the recent report on the effect of temperature on gold nanorod assembly.⁵⁵ By cycling the temperature to 80 °C and back to 20 °C (see Figure 7a), we notice two main effects: (i) the structure is robust in all thermal cycles resembling the one created in the first cycle and

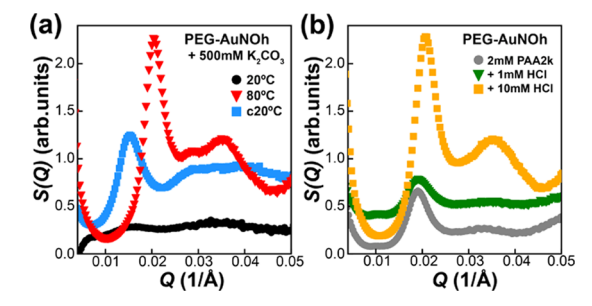


Figure 6. (a) SAXS structure factor profiles for PEG-AuNOh suspensions with 500 mM $\rm K_2CO_3$ at 20 °C (black circles, sky blue squares) and 80 °C (red triangles). Temperature is raised from 20 to 80 °C and then lowered back to 20 °C (which is labeled with $\it c20$). (b) SAXS structure factor profiles for PEG-AuNOh suspensions with 2 mM PAA2k at various pH levels at 80 °C.

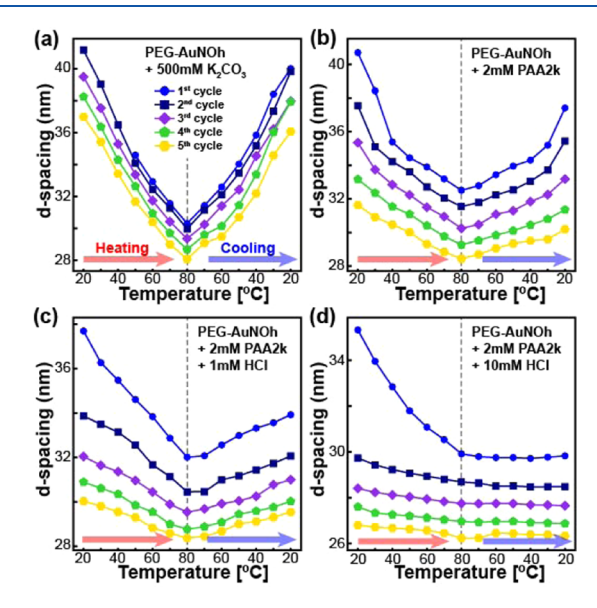


Figure 7. Interparticle distances (*d*-spacing = $2\pi/Q$) obtained from SAXS data for 3D assemblies of PEG-AuNOh with (a) 500 mM K_2CO_3 or (b–d) 2 mM PAA2k at various pH levels. One thermal cycle is implemented by raising the temperature from 20 to 80 °C and lowering it back to 20 °C. This is repeated five times for each PEG-AuNOh suspension.

exhibits almost identical thermal response; (ii) each consecutive cycle makes the 3D assemblies pack slightly denser (see the detail in Figure S12). Control experiments without K_2CO_3 are provided in Figure S13.

IPC Induced. Figure 6b shows the SAXS structure factor profiles for PEG-AuNOh suspensions at various pH levels in the presence of PAA2k at 80 °C. As is apparent in Figure 6b, the most intense and distinctive diffraction peaks are obtained from PEG-AuNOh suspensions with PAA2k at the lowest pH (~2, with 10 mM HCl). Moreover, with the increase of HCl concentration (the lowering of the pH level), Q_1 increases, indicating a denser packing of 3D assemblies with improved crystalline quality. This is consistent with previous reports that show that lower pH enhances IPC processes.^{30,55} Figure 7b shows that in the presence of PAA2k (without adding HCl), the change in interparticle distance exhibits a similar trend to that of the one of PEG-AuNOh with 500 mM K2CO3 (see more details in Figure S14). This behavior is preserved down to ~pH 3 (with 1 mM HCl, see Figure 7c and more detail in Figure S15). However, for 10 mM HCl (at pH \sim 2), the interparticle distance does not recover when the temperature is lowered from 80 to 20 °C. Overall, interparticle distance monotonically decreases in repeated temperature cycles. This, we argue, suggests that PEG-AuNOh assemblies are initially induced by PAA–PEG hydrogen bonds that by proximity develop into vdW interactions, leading to PEG dehydration and more stable and denser assembly. This is different than the observations for salt-mediated assembly (see Figure 7d and more details in Figures S16 and S17). SE We note that interparticle distance as a function of temperature shown in Figure 7 reveals that PEG-AuNOh/PAA2k assemblies formed at 10 mM HCl are the most stable with the closest interparticle distance. In the Supporting Information, we examine the likely crystal structures for PEG-AuNOh (see Figure S18).

CONCLUSIONS

Using synchrotron-based XRR, GISAXS, and SAXS techniques, we demonstrate that PEG-AuNTs and PEG-AuNOh are assembled as monoparticle layers at the vapor/liquid interface and as 3D assemblies in bulk solutions (as illustrated in Figure 1). Our results show that nonspherical, aqueous surfaceanchored PEG-AuNSts acquire preferred orientations and alignment depending on the assembly driving forces and particulate geometry. Interestingly, IPC processes induce faceto-face interactions among the PEG-AuNSts at the interface. We also demonstrate temperature-induced 3D assembly of PEG-AuNOh in the bulk with both salt-mediated and IPC strategies. We find that IPC, in general, is more effective in orienting and ordering anisotropic nanostructures, presumably by enhancing vdW interactions. These findings demonstrate that nonspherical nanostructures can be assembled to form ordered 2D or 3D structures via grafted PEG corona and induced by salts or IPC, provided the shape and size of the nanostructures are well controlled. Thus, it is anticipated that this work extends the boundaries of self-assembly of nanostructures, beyond that of isotropic nanoparticles, with potential applications in photonics and plasmonics.

ASSOCIATED CONTENT

Supporting Information

The Supporting Information is available free of charge at https://pubs.acs.org/doi/10.1021/acsanm.0c01643.

Characterization of PEG-AuNSts by DLS and UV-visible; morphology of PEG-AuNSTs; X-ray reflectivity analysis; SAXS form factor analysis of PEG-AuNSts; GISAXS intensity profiles of PEG-AuNSts with K₂CO₃; SAXS intensity profiles of PEG-AuNTs with PAA2k at various pH levels; SAXS intensity profiles of PEG-AuNOh with K₂CO₃ at various temperatures; control experiment with PEG-AuNOh in pure water; SAXS intensity profiles of PEG-AuNOh with PAA2k at various temperatures and pH levels; speculation of structure type of the 3D assemblies of PEG-AuNOh (PDF)

AUTHOR INFORMATION

Corresponding Authors

Surya K. Mallapragada — Ames Laboratory, and Department of Chemical and Biological Engineering, Iowa State University, Ames, Iowa 50011, United States; ⊙ orcid.org/0000-0002-9482-7273; Email: suryakm@iastate.edu

Wenjie Wang — Division of Materials Sciences and Engineering, Ames Laboratory, U.S. DOE, Ames, Iowa 50011, United States; orcid.org/0000-0002-7079-1691; Email: wenjiew@ameslab.gov

Authors

Hyeong Jin Kim – Ames Laboratory, and Department of Chemical and Biological Engineering, Iowa State University, Ames, Iowa 50011, United States

Md Mir Hossen — Ames Laboratory, and Department of Chemical and Biological Engineering, Iowa State University, Ames, Iowa 50011, United States; orcid.org/0000-0001-9168-4441

Andrew C. Hillier — Ames Laboratory, and Department of Chemical and Biological Engineering, Iowa State University, Ames, Iowa 50011, United States; orcid.org/0000-0002-2729-1368

David Vaknin – Ames Laboratory, and Department of Physics and Astronomy, Iowa State University, Ames, Iowa 50011, United States; orcid.org/0000-0002-0899-9248

Complete contact information is available at: https://pubs.acs.org/10.1021/acsanm.0c01643

Notes

The authors declare no competing financial interest.

ACKNOWLEDGMENTS

We thank Dr. Wei Bu at 1SID-C and the staff team at 12ID-B for synchrotron beamline support at the Advanced Photon Source. The research was supported by the U.S. Department of Energy, Office of Basic Energy Sciences, Division of Materials Sciences and Engineering. Ames Laboratory is operated for the U.S. Department of Energy by Iowa State University under Contract No. DE-AC02-07CH11358. NSF's ChemMatCARS Sector 15 is principally supported by the Divisions of Chemistry (CHE) and Materials Research (DMR), National Science Foundation, under Grant No. NSF/CHE-1834750. Use of the Advanced Photon Source, an Office of Science User Facility operated for the U.S. Department of Energy (DOE) Office of Science by Argonne National Laboratory, was supported by the U.S. DOE under Contract No. DE-AC02-06CH11357.

REFERENCES

- (1) Boles, M. A.; Engel, M.; Talapin, D. V. Self-assembly of colloidal nanocrystals: From intricate structures to functional materials. *Chem. Rev.* **2016**, *116*, 11220–11289.
- (2) Ross, M. B.; Ku, J. C.; Vaccarezza, V. M.; Schatz, G. C.; Mirkin, C. A. Nanoscale form dictates mesoscale function in plasmonic DNA-nanoparticle superlattices. *Nat. Nanotechnol.* **2015**, *10*, 453–458.
- (3) Nagaoka, Y.; Tan, R.; Li, R.; Zhu, H.; Eggert, D.; Wu, Y. A.; Liu, Y.; Wang, Z.; Chen, O. Superstructures generated from truncated tetrahedral quantum dots. *Nature* **2018**, *561*, 378–382.
- (4) Choi, J.-H.; Wang, H.; Oh, S. J.; Paik, T.; Sung, P.; Sung, J.; Ye, X.; Zhao, T.; Diroll, B. T.; Murray, B. M.; Christopher; Kagan, C. R. Exploiting the colloidal nanocrystal library to construct electronic devices. *Science* **2016**, 352, 205–208.
- (5) Ip, A. H.; Thon, S. M.; Hoogland, S.; Voznyy, O.; Zhitomirsky, D.; Debnath, R.; Levina, L.; Rollny, L. R.; Carey, G. H.; Fischer, A.; Kemp, K. W.; J, K. I.; Ning, Z.; Labelle, A. J.; Chou, K. W.; Amassian, A.; Sargent, E. H. Hybrid passivated colloidal quantum dot solids. *Nat. Nanotechnol.* **2012**, *7*, 577–582.
- (6) Kang, Y.; Ye, X.; Chen, J.; Qi, L.; Diaz, R. E.; Doan-Nguyen, V.; Xing, G.; Kagan, C. R.; Li, J.; Gorte, R. J.; Stach, E. A.; Murray, C. B. Engineering catalytic contacts and thermal stability: Gold/iron oxide binary nanocrystal superlattices for CO oxidation. *J. Am. Chem. Soc.* **2013**, *135*, 1499–1505.

- (7) Auyeung, E.; Morris, W.; Mondloch, J. E.; Hupp, J. T.; Farha, O. K.; Mirkin, C. A. Controlling structure and porosity in catalytic nanoparticle superlattices with DNA. *J. Am. Chem. Soc.* **2015**, *137*, 1658–1662.
- (8) Xu, X.; Hu, L.; Gao, N.; Liu, S.; Wageh, S.; Al-Ghamdi, A. A.; Alshahrie, A.; Fang, X. Controlled growth from ZnS nanoparticles to ZnS-CdS nanoparticle hybrids with enhanced photoactivity. *Adv. Funct. Mater.* **2015**, 25, 445–454.
- (9) Hu, K.; Chen, H.; Jiang, M.; Teng, F.; Zheng, L.; Fang, X. Broadband photoresponse enhancement of a high-performance t-Se microtube photodetector by plasmonic metallic nanoparticles. *Adv. Funct. Mater.* **2016**, *26*, *6641–6648*.
- (10) Ouyang, W.; Teng, F.; Jiang, M.; Fang, X. ZnO film UV photodetector with enhanced performance: Heterojunction with CdMoO4 microplates and the hot electron injection effect of Au nanoparticles. *Small* **2017**, *13*, No. 1702177.
- (11) Ouyang, W.; Chen, J.; He, J.-H.; Fang, X. Improved photoelectric performance of UV photodetector based on ZnO nanoparticle-decorated BiOCl nanosheet arrays onto PDMS substrate: The heterojunction and Ti3C2Tx MXene conduction layer. *Adv. Electron. Mater.* **2020**, *6*, No. 2000168.
- (12) Hsiao, H.-H.; Ke, H.; Dvoynenko, M. M.; Wang, J.-K. Multipolar resonances of Ag nanoparticle arrays in anodic aluminum oxide nanochannels for enhanced hot spot intensity and signal-to-background ratio in surface-enhanced raman scattering. ACS Appl. Nano Mater. 2020, 3, 4477–4485.
- (13) Shevchenko, E. V.; Talapin, D. V.; Kotov, N. A.; O'Brien, S.; Murray, C. B. Structural diversity in binary nanoparticle superlattices. *Nature* **2006**, 439, 55–59.
- (14) Kalsin, A. M.; Fialkowski, M.; Paszewski, M.; Smoukov, S. K.; Bishop, K. J.; Grzybowski, B. A. Electrostatic self-assembly of binary nanoparticle crystals with a diamond-like lattice. *Science* **2006**, *312*, 420–424.
- (15) Talapin, D. V.; Shevchenko, E. V.; Murray, C. B.; Titov, A. V.; Kral, P. Dipole- dipole interactions in nanoparticle superlattices. *Nano Lett.* **2007**, *7*, 1213–1219.
- (16) Nykypanchuk, D.; Maye, M. M.; Van Der Lelie, D.; Gang, O. DNA-guided crystallization of colloidal nanoparticles. *Nature* **2008**, 451, 549–552.
- (17) Park, S. Y.; Lytton-Jean, A. K.; Lee, B.; Weigand, S.; Schatz, G. C.; Mirkin, C. A. DNA-programmable nanoparticle crystallization. *Nature* **2008**, *451*, 553–556.
- (18) Macfarlane, R. J.; Lee, B.; Jones, M. R.; Harris, N.; Schatz, G. C.; Mirkin, C. A. Nanoparticle superlattice engineering with DNA. *Science* **2011**, 334, 204–208.
- (19) Zhang, Y.; Lu, F.; Yager, K. G.; Van Der Lelie, D.; Gang, O. A general strategy for the DNA-mediated self-assembly of functional nanoparticles into heterogeneous systems. *Nat. Nanotechnol.* **2013**, *8*, 865–872.
- (20) Ye, X.; Zhu, C.; Ercius, P.; Raja, S. N.; He, B.; Jones, M. R.; Hauwiller, M. R.; Liu, Y.; Xu, T.; Alivisatos, A. P. Structural diversity in binary superlattices self-assembled from polymer-grafted nanocrystals. *Nat. Commun.* **2015**, *6*, No. 10052.
- (21) Wei, J.; Schaeffer, N.; Pileni, M.-P. Ligand exchange governs the crystal structures in binary nanocrystal superlattices. *J. Am. Chem. Soc.* **2015**, 137, 14773–14784.
- (22) Mahmoud, M. A. Controlling the orientations of gold nanorods inside highly packed 2D arrays. *Phys. Chem. Chem. Phys.* **2014**, *16*, 26153–26162.
- (23) Zhang, H.; Wang, W.; Mallapragada, S.; Travesset, A.; Vaknin, D. Macroscopic and tunable nanoparticle superlattices. *Nanoscale* **2017**, *9*, 164–171.
- (24) Zhang, H.; Wang, W.; Akinc, M.; Mallapragada, S.; Travesset, A.; Vaknin, D. Assembling and ordering polymer-grafted nanoparticles in three dimensions. *Nanoscale* **2017**, *9*, 8710–8715.
- (25) Zhang, H.; Wang, W.; Mallapragada, S.; Travesset, A.; Vaknin, D. Ion-specific interfacial crystallization of polymer-grafted nanoparticles. *J. Phys. Chem. C* **2017**, *121*, 15424–15429.

- (26) Wang, W.; Zhang, H.; Mallapragada, S.; Travesset, A.; Vaknin, D. Ionic depletion at the crystalline Gibbs layer of PEG-capped gold nanoparticle brushes at aqueous surfaces. *Phys. Rev. Mater.* **2017**, *1*, No. 076002.
- (27) Horst, N.; Nayak, S.; Wang, W.; Mallapragada, S.; Vaknin, D.; Travesset, A. Superlattice assembly by interpolymer complexation. *Soft Matter* **2019**, *15*, 9690–9699.
- (28) Wang, W.; Kim, H. J.; Bu, W.; Mallapragada, S. K.; Vaknin, D. Unusual effect of iodine ions on the self assembly of poly-ethylene glycol capped gold nano-particles. *Langmuir* **2020**, *36*, 311–317.
- (29) Wang, W.; Lawrence, J. J.; Bu, W.; Zhang, H.; Vaknin, D. Two-dimensional crystallization of poly (N-isopropylacrylamide)-capped gold nanoparticles. *Langmuir* **2018**, *34*, 8374–8378.
- (30) Nayak, S.; Horst, N.; Zhang, H.; Wang, W.; Mallapragada, S.; Travesset, A.; Vaknin, D. Interpolymer complexation as a strategy for nanoparticle assembly and crystallization. *J. Phys. Chem. C* **2019**, *123*, 836–840.
- (31) Nayak, S.; Fieg, M.; Wang, W.; Bu, W.; Mallapragada, S.; Vaknin, D. Effect of (poly) electrolytes on the interfacial assembly of poly (ethylene glycol)-functionalized gold nanoparticles. *Langmuir* **2019**, 35, 2251–2260.
- (32) Nikoobakht, B.; Wang, Z.; El-Sayed, M. Self-assembly of gold nanorods. *J. Phys. Chem. B* **2000**, *104*, 8635–8640.
- (33) Dujardin, E.; Hsin, L.-B.; Wang, C. C.; Mann, S. DNA-driven self-assembly of gold nanorods. *Chem. Commun.* **2001**, 1264–1265.
- (34) Sreeprasad, T. S.; Samal, A.; Pradeep, T. One-, two-, and three-dimensional superstructures of gold nanorods induced by dimercaptosuccinic acid. *Langmuir* **2008**, *24*, 4589–4599.
- (35) Grzelczak, M.; Rodríguez-González, B.; Pérez-Juste, J.; Liz-Marzán, L. M. Quasi-epitaxial growth of Ni nanoshells on Au nanorods. *Adv. Mater.* **2007**, *19*, 2262–2266.
- (36) Tao, A.; Kim, F.; Hess, C.; Goldberger, J.; He, R.; Sun, Y.; Xia, Y.; Yang, P. Langmuir-Blodgett silver nanowire monolayers for molecular sensing using surface-enhanced Raman spectroscopy. *Nano Lett.* **2003**, *3*, 1229–1233.
- (37) Bae, Y.; Kim, N. H.; Kim, M.; Lee, K. Y.; Han, S. W. Anisotropic assembly of Ag nanoprisms. *J. Am. Chem. Soc.* **2008**, *130*, 5432–5433.
- (38) Rycenga, M.; McLellan, J. M.; Xia, Y. Controlling the assembly of silver nanocubes through selective functionalization of their faces. *Adv. Mater.* **2008**, *20*, 2416–2420.
- (39) Chen, M.; Kim, J.; Liu, J.; Fan, H.; Sun, S. Synthesis of FePt nanocubes and their oriented self-assembly. *J. Am. Chem. Soc.* **2006**, 128, 7132–7133.
- (40) Saunders, A. E.; Ghezelbash, A.; Smilgies, D.-M.; Sigman, M. B.; Korgel, B. A. Columnar self-assembly of colloidal nanodisks. *Nano Lett.* **2006**, *6*, 2959–2963.
- (41) Huang, T.; Zhao, Q.; Xiao, J.; Qi, L. Controllable self-assembly of PbS nanostars into ordered structures: Close-packed arrays and patterned arrays. ACS Nano 2010, 4, 4707–4716.
- (42) Pastoriza-Santos, I.; Liz-Marzán, L. M. Colloidal silver nanoplates. State of the art and future challenges. *J. Mater. Chem.* **2008**, *18*, 1724–1737.
- (43) Xue, C.; Métraux, G. S.; Millstone, J. E.; Mirkin, C. A. Mechanistic study of photomediated triangular silver nanoprism growth. *J. Am. Chem. Soc.* **2008**, *130*, 8337–8344.
- (44) Schnepf, M. J.; Mayer, M.; Kuttner, C.; Tebbe, M.; Wolf, D.; Dulle, M.; Altantzis, T.; Formanek, P.; Förster, S.; Bals, S.; König, T. A. F.; Fery, A. Nanorattles with tailored electric field enhancement. *Nanoscale* **2017**, *9*, 9376–9385.
- (45) O'Brien, M. N.; Jones, M. R.; Lee, B.; Mirkin, C. A. Anisotropic nanoparticle complementarity in DNA-mediated co-crystallization. *Nat. Mater.* **2015**, *14*, 833–839.
- (46) Lin, Q.-Y.; Li, Z.; Brown, K. A.; O'Brien, M. N.; Ross, M. B.; Zhou, Y.; Butun, S.; Chen, P.-C.; Schatz, G. C.; Dravid, V. P.; et al. Strong coupling between plasmonic gap modes and photonic lattice modes in DNA-assembled gold nanocube arrays. *Nano Lett.* **2015**, *15*, 4699–4703.

- (47) Kim, H. J.; Wang, W.; Bu, W.; Hossen, M. M.; Londono-Calderon, A.; Hillier, A. C.; Prozorov, T.; Mallapragada, S.; Vaknin, D. Salt mediated self-assembly of poly (ethylene glycol)-functionalized gold nanorods. *Sci. Rep.* **2019**, *9*, No. 20349.
- (48) Kuttner, C.; Mayer, M.; Dulle, M.; Moscoso, A.; López-Romero, J. M.; Förster, S.; Fery, A.; Pérez-Juste, J.; Contreras-Cáceres, R. Seeded growth synthesis of gold nanotriangles: Size control, SAXS analysis, and SERS performance. ACS Appl. Mater. Interfaces 2018, 10, 11152–11163.
- (49) Casado-Rodriguez, M.; Sanchez-Molina, M.; Lucena-Serrano, A.; Lucena-Serrano, C.; Rodriguez-Gonzalez, B.; Algarra, M.; Diaz, A.; Valpuesta, M.; Lopez-Romero, J. M.; Perez-Juste, J.; Contreras-Caceres, R. Synthesis of vinyl-terminated Au nanoprisms and nanooctahedra mediated by 3-butenoic acid: Direct Au@ pNIPAM fabrication with improved SERS capabilities. *Nanoscale* **2016**, *8*, 4557–4564.
- (50) Scarabelli, L.; Sánchez-Iglesias, A.; Pérez-Juste, J.; Liz-Marzán, L. M. A "tips and tricks" practical guide to the synthesis of gold nanorods. *J. Phys. Chem. Lett.* **2015**, *6*, 4270–4279.
- (51) Khlebtsov, B.; Khlebtsov, N. On the measurement of gold nanoparticle sizes by the dynamic light scattering method. *Colloid J.* **2011**, 73, 118–127.
- (52) Jana, N. R. Nanorod shape separation using surfactant assisted self-assembly. *Chem. Commun.* **2003**, 1950–1951.
- (53) Hossen, M. M.; Bendickson, L.; Palo, P. E.; Yao, Z.; Nilsen-Hamilton, M.; Hillier, A. C. Creating metamaterial building blocks with directed photochemical metallization of silver onto DNA origami templates. *Nanotechnology* **2018**, *29*, No. 355603.
- (54) Als-Nielsen, J.; McMorrow, D. Elements of Modern X-ray Physics; John Wiley & Sons, 2011.
- (55) Kim, H. J.; Wang, W.; Travesset, A.; Mallapragada, S. K.; Vaknin, D. Temperature-induced tunable assembly of columnar phases of nanorods. *ACS Nano* **2020**, *14*, 6007–6012.
- (56) Vaknin, D. X-ray Diffraction and Spectroscopic Techniques from Liquid Surfaces and Interfaces. In *Characterization of Materials*, 2nd ed.; Kaufmann, E. N., Ed.; John Wiley & Sons, 2012; Vol. 2, pp 1393–1423.
- (57) Pershan, P. S.; Schlossman, M. Liquid Surfaces and Interfaces: Synchrotron X-ray Methods; Cambridge University Press, 2012.
- (58) Michaels, A. S.; Morelos, O. Polyelectrolyte adsorption by kaolinite. *Ind. Eng. Chem.* **1955**, 47, 1801–1809.
- (59) Wiśniewska, M.; Urban, T.; Grządka, E.; Zarko, V. I.; Gun'ko, V. M. Comparison of adsorption affinity of polyacrylic acid for surfaces of mixed silica-alumina. *Colloid Polym. Sci.* **2014**, 292, 699–705
- (60) Guinier, A.; Fournet, G.; Yudowitch, K. L. Small-Angle Scattering of X-rays; Wiley: New York, 1955.